A multiscale insight into the growth of h-BN: effect of the enclosure

2D Materials

PAPER

A multiscale insight into the growth of h-BN: effect of the enclosure

RECEIVED
17 March 2021

REVISED
20 April 2021

ACCEPTED FOR PUBLICATION
28 April 2021

PUBLISHED
13 May 2021

Yanzhou Ji[1,3], Kasra Momeni[1,2,3,*] and Long-Qing Chen[1,*]

[1] Department of Materials Science and Engineering, The Pennsylvania State University, University Park, PA 16802, United States of America
[2] Department of Mechanical Engineering, University of Alabama, Tuscaloosa, AL 35487, United States of America
[3] These authors have equal contributions.
[*] Authors to whom any correspondence should be addressed.

E-mail: kmomeni@ua.edu **and** lqc3@psu.edu

Keywords: hexagonal boron nitride (h-BN), chemical vapor deposition (CVD), phase-field, 2D materials, materials synthesis

Supplementary material for this article is available online

Abstract

There is a lack of knowledge on the fundamental growth mechanisms governing the characteristics of 2D materials synthesized by the chemical vapor deposition (CVD) technique and their correlation with experimentally controllable parameters, which hindered their wafer-scale synthesis. Here, we pursued an analytical and computational approach to access the system states that are not experimentally viable to address these critical needs. We developed a multiscale computational framework correlating the macroscale heat and mass flow with the mesoscale morphology of the as-grown 2D materials by solving the coupled system of heat/mass transfer and phase-field equations. We used hexagonal boron nitride (h-BN) as our model material and investigated the effect of substrate enclosure on its growth kinetics and final morphology. We revealed a lower concentration with a more uniform distribution on the substrate in an enclosed-growth than open-growth. It leads to a more uniform size distribution of the h-BN islands, consistent with existing experimental investigations.

1. Introduction

Atomically thin hexagonal boron nitride (h-BN) has a wide bandgap (~5.95 eV) [1], high thermal conductivity [2], good mechanical strength [3], and chemical stability [4]. It has several potential applications [5–7], including dielectric layers, heat exchangers, substrates in flexible electronics [8] and energy storage devices [9], and oxidation-resistant coatings of metals [4]. A vital precondition to realize these functionalities and applications is the controllable and scalable synthesis of h-BN. Specifically, its size, morphology, and number of layers should be carefully controlled [10].

Chemical vapor deposition (CVD)-based techniques are the most promising for synthesizing wafer-scale high-quality 2D materials, such as h-BN, graphene, and transition metal dichalcogenides (TMDs). This interest is due to the versatility and the vast space of control parameters of CVD growth. The effects of growth conditions on the morphology of CVD-grown h-BN have been experimentally investigated, including the type of precursor [11–13], substrate [11, 14–17], growth temperature [16, 18, 19], precursor sublimation temperature [18, 20–22], carrier gas type [23], pressure [24], flow rate [18], and growth time. These studies have shown that the h-BN island size, shape, orientation, number of layers, and growth kinetics are directly related to the macroscopic control variables. Large-area growth of high-quality h-BN has been reported [3, 25, 26]. However, synthesis by design and transferability of the growth parameters from one system to another is still a challenge because of the extended design space and the h-BN morphology's sensitivity to the subtle changes in growth conditions. Furthermore, it is extremely challenging to fully understand the underlying growth mechanisms of h-BN via pure experimentation due to the complicated interactions among the physical and chemical processes.

Theoretical calculations and computer simulations at different length and temporal scales have

been used to explain the experimentally observed growth morphologies of h-BN. These tools, ranging from atomistic-scale first-principles calculations and molecular dynamics (MD) simulations to mesoscale kinetic Monte Carlo and phase-field approaches to macroscopic heat transfer and fluid dynamics, could shed light on the mechanisms governing the growth of 2D materials and guide the experimental growth [27–29]. An extensive review of these methods is presented in [30]. Density functional theory (DFT) has been applied to calculate the anisotropic edge energies of h-BN under different atmospheres (B-rich, N-rich, and exposure to H_2) [31–35], energy change for h-BN islands with different orientations on the substrate [36], and formation energy of h-BN clusters on Cu substrate [37], which could predict the equilibrium shape, orientation, and early-stage geometry of h-BN nano-islands. MD simulations, including both *ab initio* MD [38] and reactive MD [39–41] techniques, have been applied to investigate the nucleation mechanisms and nanoscale island morphologies of h-BN and similar 2D materials during CVD. Phase-field simulations [42–45] have been performed to explain the experimentally observed h-BN morphologies in terms of the competition between deposition and edge diffusion [16, 46]. However, most of these existing studies focus on one or a few aspects of CVD growth, and no attempts exist to correlate the h-BN growth morphology with macroscopic CVD parameters.

Recently, multiscale and multiphysics approaches were developed for the CVD growth of 2D materials [43, 47]. These methods capture the governing growth mechanisms at the respective length/time scale, semi-quantitatively reproduce the experimentally observed growth morphology, and directly relate the growth morphology with CVD parameters. Such an approach can potentially be an alternative to the costly and time-consuming trial-and-error experimentations.

Here, we developed a multiscale model for the CVD growth of h-BN. The macroscopic growth chamber model predicts the precursor concentration distribution on the substrate, which is then passed to the mesoscale phase-field model and combined with existing DFT-calculated edge energies to predict the morphology of h-BN. The effect of an enclosure and its geometry on the size, morphology, distribution, and growth kinetics of h-BN islands is investigated and compared qualitatively with existing experimental results.

2. The multiscale model formulation

The proposed multiscale model integrates the macroscale model of heat and mass transfer and the mesoscale phase-field model of the growth. We apply the model to the low-pressure CVD growth of h-BN on a Cu (111) substrate at 1050 °C, using ammonia borane (AB) as the precursor following the process elaborated in [10]. We used this model to systematically investigate the effect of encapsulation with copper foil on the growth morphology.

2.1. Macroscale model of the growth chamber

The current macroscale multiphysics model predicts the spatial distribution of precursor concentration, carrier gas velocity, pressure, and temperature within the CVD growth chamber by coupling the mass flow (Navier–Stokes), heat transfer (conduction and convection), and flow-assisted mass transport [28, 29, 43] equations, respectively, i.e.

$$\rho\frac{\partial \mathbf{v}}{\partial t}+\rho(\mathbf{v}\cdot\nabla)\mathbf{v}=\nabla\cdot\left[-p\mathbf{I}+\mu\left(\nabla\mathbf{v}+(\nabla\mathbf{v})^{T}\right)\right]+\mathbf{F}_{\mathrm{b}}, \tag{1}$$

$$\rho C_{\mathrm{p}}\frac{\partial T}{\partial t}+\rho C_{\mathrm{p}}\mathbf{v}\cdot\nabla T=\nabla\cdot(k\nabla T)+Q \tag{2}$$

$$\frac{\partial c}{\partial t}+\mathbf{v}\cdot\nabla c=\nabla\cdot(D\nabla c)+R. \tag{3}$$

We assume incompressible flow, so $\rho\nabla\cdot\mathbf{v}=0$. Here, ρ is the density, $\mathbf{v}$ is the velocity field, p is the pressure, μ is the dynamic viscosity, $\mathbf{I}$ is the identity matrix, $\mathbf{F}_{\mathrm{b}}$ is the body force, c_{p} is the heat capacity at constant pressure, T is temperature, k is thermal conductivity, Q is the heat source, c is the precursor concentration, D is the diffusion coefficient in the gas phase, and R is the source term (e.g. reaction).

These coupled equations are applied to the furnace chamber for h-BN growth. The chamber is a tube with a diameter of 4 cm and a length of 107 cm, where the mixture of AB precursor and carrier gas argon enters it from a mixing chamber via a valve with a 1.5 cm diameter. The substrate has a length of 1.8 cm and a height of 1 mm, located at the center of the furnace. We developed a 2D model to keep the computational costs tractable. The model configuration is presented in figure 1(a). The parameter values for the growth of h-BN are listed in table 1, and the boundary conditions are listed in table 2. We have normalized the precursor concentration with its value at the source for our simulations. The absolute value of the precursor concentration in the experiments is in the order of a few μg cc^{-1}. Temperature distribution over the furnace walls is measured from experiments and shown in figure 1(b). Temperature-dependent physical quantities are shown in figure S1 of supplementary materials (available online at stacks.iop.org/2DM/8/035033/mmedia). The governing equations equations (1)–(3) are solved using the finite element method and implemented in COMSOL Multiphysics.

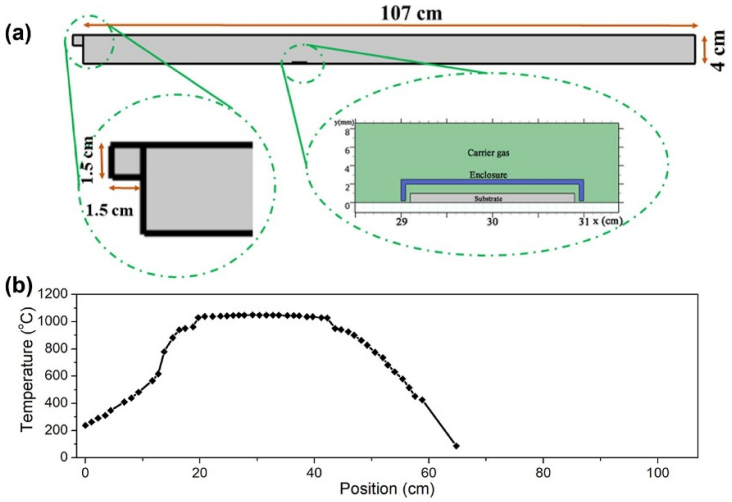

Figure 1. Furnace configuration and temperature distribution. (a) Geometry and configuration of the macroscale model for the growth chamber. The enlarged figure on the left shows the valve; the enlarged figure on the right shows the substrate and enclosure. (b) Temperature distribution over the wall of the growth chamber. The origin of the coordinate system is located at the entrance of the chamber.

Table 1. Parameters of the macroscale model of heat and mass transport in the furnace.

Parameters	Description	Values [units]
p_i	Initial chamber pressure	0.1[Torr]
p_o	Outlet pressure	0.1[Torr]
V_{pre}	Precursor inlet	1 [cc min^{-1}]
A_{pre}	Precursor inlet area	7.0686 [cm^2]
V_{Ar}	Argon inlet	12 [cc min^{-1}]
A_{Ar}	Argon inlet area	7.0686 [cm^2]
ρ	Carrier gas density	See figure S1
C_p	Carrier gas heat capacity	See figure S1
k	Carrier gas thermal conductivity	See figure S1
μ	Carrier gas dynamic viscosity	See figure S1
γ	Carrier gas specific heat ratio	1.66

Table 2. Boundary conditions for the heat and mass transfer equations (1)–(3).

Navier–Stokes	
No-slip on walls	$\mathbf{v} = 0$
Normal inflow velocity	$\mathbf{v} = -V_0 \cdot \mathbf{n}$
Zero outlet pressure	$-p\boldsymbol{I} + \mu\left(\nabla\mathbf{v} + (\nabla\mathbf{v})^{\mathrm{T}}\right) - \frac{2}{3}\mu(\nabla\cdot\mathbf{v})\mathbf{I} = 0$
Heat transfer	
Inlet	$-\mathbf{n}\cdot(-k\nabla T) = 0$
Outflow	$-\mathbf{n}\cdot(-k\nabla T) = 0$
On furnace wall	See figure 1(b)
Flow assisted diffusion	
No flux at furnace walls	$-\mathbf{n}\cdot\mathbf{N}_i = 0$
Concentration @ source	Constant c_0
Outflow	$-\mathbf{n}\cdot D_i\nabla c_i$
Inflow	$c = 0$

Here $\mathbf{N}_i = -D_i\nabla c_i + \mathbf{v}c_i$ is the flow-assisted diffusion flux.

The solution to the coupled system of equations (1)–(3) provides information on the distribution and temporal variation of precursor concentration, temperature, pressure, and flow rates within the furnace. We pass the calculated precursor concentration distribution to the phase-field model to calculate the distribution and morphology of the h-BN. Specifically, the concentration of precursors in the gas phase in the vicinity of the substrate—i.e. the value of precursor concertation on the boundary of the volume representing the gas phase—is used as the input of the phase-field model. We neglect the change in precursor concentration in the gas phase due to the deposition and growth of h-BN on the substrate.

The proposed model only takes into account the flow-assisted diffusion of the precursors and neglects the chemical reactions and breakdown of species. Implementation of these reactions requires a comprehensive knowledge of the gas phase reaction kinetics, which requires atomistic simulations such as nudged elastic band calculations [31, 32], *ab initio* MD simulations [38], and reactive MD simulations [39, 40]. We expect that implementing the gas-phase reactions will reduce the predicted fluid temperature, as reactions act as the heat sink. We also defined the edge energies as functions of precursor concentrations, which can be defined as functions of a specific reaction product in the reactive flow model.

2.2. Mesoscale phase-field model

2.2.1. Model description

The mesoscale phase-field model simulates the growth morphology of h-BN on a substrate. The model is based on the Burton–Cabrera–Frank theory [48] and extended from existing phase-field models [42–44]. We made the following simplifying assumptions: (a) the detailed chemical reactions to form h-BN are neglected, and the growth process is simplified as the deposition of solid-state h-BN from supersaturated h-BN gas; (b) the effect of chemical potential difference on edge energies is neglected due to the fixed (1:1) B:N ratio of the precursor and the precursor is neither B-rich nor N-rich; (c) multilayer h-BN growth is neglected; (d) the effect of elasticity and plasticity of the system originated from the island/substrate misfit strain is neglected due to the weak van der Waals interaction between Cu and h-BN, the relatively small mismatch between Cu (111) and h-BN, and the high computation cost for considering elasticity/plasticity on the whole substrate; and (e) the temperature is assumed uniform on the substrate as shown by the relatively flat temperature distribution in figure 1(b) neat the substrate (29–31 cm). Thus, the growth process can be described using two sets of continuously varying phase-field variables: the order parameter ϕ to distinguish the substrate ($\phi = -1$) and the h-BN island ($\phi = 1$), and the reduced saturation field u to describe concentration distribution. u is related to the precursor concentration c by $u = (c - c_{eq})/c_{eq}$, where c_{eq} is the equilibrium concentration at a given temperature and pressure. Consider a system containing several orientations of h-BN, the total free energy $\mathcal{F}$ of the system can be formulated as

$$\mathcal{F} = \int_V \in \left[f(\phi_i) - \lambda u g(\phi_i) + \frac{1}{2}\sum_i W(\theta_i)^2 (\nabla\phi_i)^2 \right] \mathrm{d}V, \quad (4)$$

where each subscript i represents one specific lattice orientation of the h-BN island with respect to the substrate; $\in$ is an energy scale, λ is the coupling coefficient between ϕ and u; $f(\phi_i) = \sum_i \left(\phi_i^2 - 1\right)^2 + \alpha \sum_{i \neq j} (\phi_i + 1)^2 (\phi_j + 1)^2$ is a double-well-type function with α being a positive constant to avoid the coexistence of two different island orientations at the same location; $g(\phi_i) = \frac{\phi_i^5}{5} - \frac{2\phi_i^3}{3} + \phi_i$ is an interpolation function; $W(\theta_i) = W_0 a(\theta_i)$ is the orientation-dependent interface thickness where $\theta_i = \arctan\left(\frac{\partial_y \phi_i}{\partial_x \phi_i}\right)$ is the local surface orientation angle and $a(\theta_i)$ is the anisotropy function.

The governing kinetic equations include the Allen–Cahn equations for ϕ_i and diffusion equation for u,

$$\frac{1}{L(\theta_i) \in}\frac{\partial \phi_i}{\partial t} = -\frac{1}{\in}\frac{\delta \mathcal{F}}{\delta \phi_i} = -f'(\phi_i) + \lambda u g'(\phi_i) + \nabla \cdot \left[W(\theta_i)^2 \nabla \phi_i \right] - \nabla \cdot \left[W(\theta_i) \cdot W'(\theta_i) \frac{\partial \theta_i}{\partial (\nabla \phi_i)} \right], \quad (5)$$

$$\frac{\partial u}{\partial t} = \nabla \cdot \left[\mathbf{D}(\phi_i) \nabla u \right] + \frac{1 - h(\{\phi_i\})}{2} F - \frac{1}{2}\sum_i \frac{\partial \phi_i}{\partial t}. \quad (6)$$

Here, $L(\theta_i)$ is an orientation-dependent interface kinetic coefficient, $\mathbf{D}(\phi_i)$ is a symmetric diffusion matrix, containing the substrate diffusivity contribution $\mathbf{D^s}$ and edge diffusivity contribution $\mathbf{D^e}$: $\mathbf{D}(\phi_i) = \frac{1-h(\{\phi_i\})}{2}\mathbf{D^s} + \left[1 - h(\{\phi_i\})^2\right]\mathbf{D^e}$, where $h(\{\phi_i\}) = -1 + \sum_i (1 + \phi_i)$ is another interpolation function. In principle, $\mathbf{D^s}$ and $\mathbf{D^e}$ are all matrices; for example, $\mathbf{D^s} = \begin{pmatrix} D^s_{xx} & D^s_{xy} \\ D^s_{xy} & D^s_{yy} \end{pmatrix}$. The expression $\nabla \cdot [\mathbf{D}(\phi_i)\nabla u]$ can also be written as $\nabla_j \left[D_{jk}(\phi_i)\nabla_k u\right]$ in Einstein notation, where $j, k = x, y$. The components D^s_{xx}, D^s_{xy} and D^s_{yy} of the diffusivity matrix are different depending on the crystal symmetry of the substrate surface. F is the deposition rate of the adatoms. F can be connected to precursor breakdown reaction parameters evaluated from reactive MD simulations. Note that the function $\frac{1-h(\{\phi_i\})}{2}$ guarantees that D_s and F vanish inside the islands, while $\left[1 - h(\{\phi_i\})^2\right]$ guarantees that D_e only contributes to the edges. The governing phase-field equations are solved using the finite difference method and our in-house Fortran code that is parallelized using the message passing interface (MPI) standard.

To account for the nucleation of h-BN islands, an explicit nucleation algorithm [49] based on classical nucleation theory and Poisson seeding is introduced. The nucleation rate I at any given time and position can be calculated as

$$I = I_0 \exp\left(-\frac{\beta_{het}\Delta G^*}{k_B T}\right), \quad (7)$$

where I_0 is a prefactor related to atom jump frequency and available nucleation sites, ΔG^* is the activation energy for nucleation, k_B is the Boltzmann constant and β_{het} is a parameter characterizing the level of heterogeneous nucleation. Given the total free energy function in equation (4) and assuming the nucleation of a circular island, the critical nucleus size r^* and nucleation barrier ΔG^* can be calculated by

$$r^* = -\frac{4\sqrt{2}W_0}{3\lambda u\left[g(-1) - g(1)\right]} \quad (8a)$$

$$\Delta G^* = -\frac{32\pi \in W_0^2}{9\lambda u\left[g(-1) - g(1)\right]}. \quad (8b)$$

Nucleation can only happen if the precursor is supersaturated (i.e. $u > 0$). The nucleation probability P can then be calculated as

$$P = 1 - \exp(-I \cdot \Delta t). \quad (9)$$

At each grid point, P is calculated and compared with a random number; if the random number is smaller than P, a nucleus with the critical radius r^* is introduced. It should be noted that r^* decreases with the increase of u, which may be smaller than the interface width W_0. However, by properly adjusting β_{het}, nucleation can take place at proper saturation levels with r^* larger than W_0. Of course, this treatment may ignore the island nucleation and growth process at nanoscales. Still, it also greatly reduces the computation cost for simulating island nucleation, growth, and coarsening behaviors on the whole substrate. A more accurate treatment may be developing a multiscale simulation approach for nucleation and growth of islands at different length scales and then combine these simulations. This approach should start from phase-field simulations at nanoscales for selected small regions on the substrate. Then gradually increase the simulation size when the island size increases in the simulation region until the simulation size scale becomes large enough to capture the growth behavior on the whole substrate. We will develop such a multiscale scheme in the near future.

2.2.2. Parameterization

The phase-field model's key parameters that determine the morphology and growth kinetics of the h-BN islands can be classified into two categories, i.e. thermodynamic and kinetic parameters. According to 1D analytical solutions of the phase-field model, the thermodynamic parameter $\in$ and orientation-dependent interface thickness $W(\theta_i)$ are related to the anisotropic edge energy $\gamma(\theta_i)$ via $\frac{4\sqrt{2}}{3} \in W(\theta_i) = \gamma(\theta_i)$. Meanwhile, $\gamma(\theta_i)$, a critical parameter for the h-BN island shape, can be obtained from DFT calculations. $\gamma(\theta_i)$ for arbitrary orientations is typically expressed as [34]

$$\gamma(\theta_i) = 2\sqrt{\gamma_{AC}^2 + \gamma_{ZZ-x}^2 - \sqrt{3}\gamma_{AC}\gamma_{ZZ-x}}\cos \times \left(\theta_i + \mathrm{sgn}(\theta_i) \cdot \arctan\left(\sqrt{3} - \frac{2\gamma_{ZZ-x}}{\gamma_{AC}}\right)\right), \quad (10)$$

where γ_{AC} is the edge energy of the armchair (AC) edge (located at 0°, ±60°, ±120°, ±180°), γ_{ZZ-x} is the zigzag (ZZ) edge energy with x (x = B, N) terminations. The ZZ-B edges are located at 30°, 150°, and −90°, while the ZZ-N edges are located at 90°, −30°, and −150°. However, equation (10) is not a smooth function of θ_i. To avoid missing orientations in phase-field simulations, we use $a(\theta_i) = a_0\left\{1 + a_1\sqrt{f_0 + \cos^2\left[\frac{3}{2}\left(\theta_i - \theta_i^0 + \frac{\pi}{2}\right)\right]} + a_2\sqrt{f_0 + \sin^2\left[\frac{3}{2}\left(\theta_i - \theta_i^0 + \frac{\pi}{2}\right)\right]}\right\}$, where $f_0 = 0.001$ is a small regularization value (0.001 for this study), θ_i^0 is the initial island orientation, while the coefficients a_0, a_1, and a_2 are fitted from existing DFT calculations [31–34] so that at $\theta_i^0 = 0$, $\frac{4\sqrt{2}}{3} \in W(0) = \gamma_{AC}$, $\frac{4\sqrt{2}}{3} \in W\left(\frac{\pi}{2}\right) = \gamma_{ZZ\text{-}N}$ and $\frac{4\sqrt{2}}{3} \in W\left(\frac{\pi}{6}\right) = \gamma_{ZZ-B}$. These coefficients are listed in table 3. In addition, the grain boundary (GB) energy between islands with different orientations can affect the coarsening rate, which, in the current model, is controlled by the parameter α in the expression of $f(\phi_i)$. In reality, this GB energy should be a function of the misorientation angle between adjacent islands, as described by the Read–Shockley equation. In the current study, we consider high angle GBs with misorientation angles higher than 15° (see the difference between different θ_i^0 values in table 3), whose GB energy is typically independent of misorientation angles. Therefore, we only consider a constant α value in the simulation. More accurate consideration of the GB energies, especially those between islands with lower misorientation angles, would rely on atomistic simulations.

The kinetic parameters in the phase-field model include the diffusion coefficients, the interface's

Table 3. Parameters used in phase-field simulations.

Parameters	Description	Values [units]
$\in$	Energy scale	1.021×10^{-4} [J m^{-2}]
λ	Coupling coefficient	15.96
c_{eq}	Equilibrium precursor concentration	10^{-9} [mol m^{-3}]
W_0	Interface thickness	5 [μm]
α	Constant in $f(\phi_i)$	10.0
a_0, a_1, a_2, f_0	Fitting coefficients in $a(\theta_i)$	1.0, 0.2047, −0.343, 0.001
$a_{L0}, a_{L1}, a_{L2}, f_{L0}$	Fitting coefficients in $a_L(\theta_i)$	−2.6912, −0.968 901, −0.968 876, 0.001
D^e/D^s	Ratio between edge and substrate diffusivities	10
Δt^*	Time step size	0.01
L_0	Prefactor of interface kinetic coefficient	3.92×10^4 [m^2 J^{-1} s^{-1}]
F	Deposition rate	10^{-4} [s^{-1}]
I_0	Prefactor of nucleation rate	1 [m^{-3} s^{-1}]
β_{het}	Heterogeneous nucleation factor	5×10^{-5}
θ_i^0	Initial island orientations	0, $\frac{\pi}{12}$, $-\frac{\pi}{12}$, $\frac{\pi}{6}$, $-\frac{\pi}{6}$, $\frac{\pi}{4}$

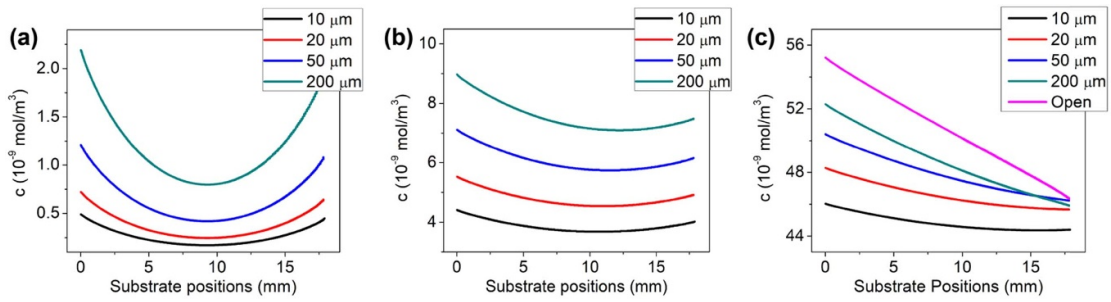

Figure 2. Precursor concentration distribution on the substrate for different opening sizes. (a) Diffusivity 10^3 cm^2 s^{-1}. (b) Diffusivity 10^4 cm^2 s^{-1}. (c) Diffusivity 10^5 cm^2 s^{-1}. The zero position is on the edge of the substrate located in the flow upstream.

kinetic coefficient $L(\theta_i)$, and deposition rate, as listed in table 3. Specifically, $L(\theta_i)$ can be expressed in a similar way to that of $W(\theta_i)$, i.e. $L(\theta_i) = L_0 a_L(\theta_i) = L_0 a_{L0}\left\{1 + a_{L1}\sqrt{f_{L0} + \cos^2\left[\frac{3}{2}\left(\theta_i - \theta_i^0 + \frac{\pi}{2}\right)\right]} + a_{L2}\sqrt{f_{L0} + \sin^2\left[\frac{3}{2}\left(\theta_i - \theta_i^0 + \frac{\pi}{2}\right)\right]}\right\}$, where $f_{L0} = 0.001$ is a small regularization value while a_{L0}, a_{L1}, and a_{L2} are fitting coefficients. Neglecting the diffusion of B and N monomers and BN dimers, the kinetic coefficient $L(\theta_i)$ is proportional to the interface velocity, and the coefficients L_0, L_1, and L_2 can be obtained from the DFT-predicted interface velocities of principal h-BN edges [34]. It should be noted that in real cases, both the diffusivity and edge mobility can determine the h-BN edge velocities, which the current phase-field model could well address. The diffusivity values determine the time scale of the current simulation. We convert the simulation time step size Δt^* (in reduced unit) to real-time interval Δt via $\Delta t = W_0^2 \Delta t^* / D^s$. This conversion will become more quantitative once an accurate estimation of the substrate diffusivity D^s is reported. In addition, we assume the edge diffusivity D^e is 10 times higher than D^s due to the higher concentration of defects at edges.

3. Results and discussions

3.1. Precursor distribution in the growth chamber

Improvement in the growth quality of both graphene [50] and h-BN [10, 51] has been reported by encapsulating the substrate, where larger and more uniform 2D nano-islands formed. Here, we investigate the effect of precursor diffusivity and encapsulation and its openings' size on the precursor concentration distribution over the substrate. Our results revealed that the precursor concentration over the substrate reduces and becomes more uniform for a fixed diffusivity as the opening size reduces, see figure 2. Furthermore, increasing the diffusivity of precursor, e.g. by reducing the growth chamber pressure while fixing the opening size, leads to higher and more uniform precursor concentrations. For the same diffusivity, the precursor concentration distributions follow a similar pattern for different opening sizes. The substrate's left boundary, which is located upstream, typically has the highest precursor concentration. However, the position of the lowest precursor concentration moves from the center of the substrate to the right boundary with the increase of the diffusivity. This is due to the dominance of flow-assisted diffusion upstream due to higher velocity, while in the downstream, pure diffusion is the driving force for penetration of precursor into the encapsulated volume. The average value of concentration increases by increasing the diffusivity of the precursor and the size of the opening. The on-coming velocity of the BN precursor to the substrate is not only higher in the case of an open substrate, but it is also nonuniform and varies drastically normal to the substrate.

3.2. Growth morphology and kinetics

3.2.1. Growth morphology of a single island

The growth morphology and kinetics of h-BN are governed by several factors, including adatom deposition and desorption, substrate and edge diffusivities, the precursor saturation, and the anisotropies in edge energy, diffusivity, and mobility. These effects are included in the current phase-field model, predicting the growth morphology of h-BN using the CVD technique. To validate the model, we first simulated the growth of an initially circular h-BN nucleus under given, uniform initial saturation and zero deposition rate, with the anisotropic edge energies and mobilities took from existing DFT calculations and without nucleation of additional h-BN islands in the system. Although several sets of h-BN edge energies are reported, we use the data by Zhang *et al* [34] considering the effect of Cu (111) substrates and the activation energies of principal edges. Under $\Delta\mu = 0$, several different combinations of anisotropies are considered for h-BN growth on Cu (111): (a) only edge energy anisotropy; (b) only edge mobility anisotropy; and (c) both edge energy and mobility anisotropies. With only the edge energy anisotropy, the shape of the island will gradually change from circular to equilaterally triangular with rounded convex corners (figure 3(d)), with the long edge being the ZZ-N edge, which is consistent with the prediction from Wulff constructions shown by the red line in figure 3(a). With only the edge mobility

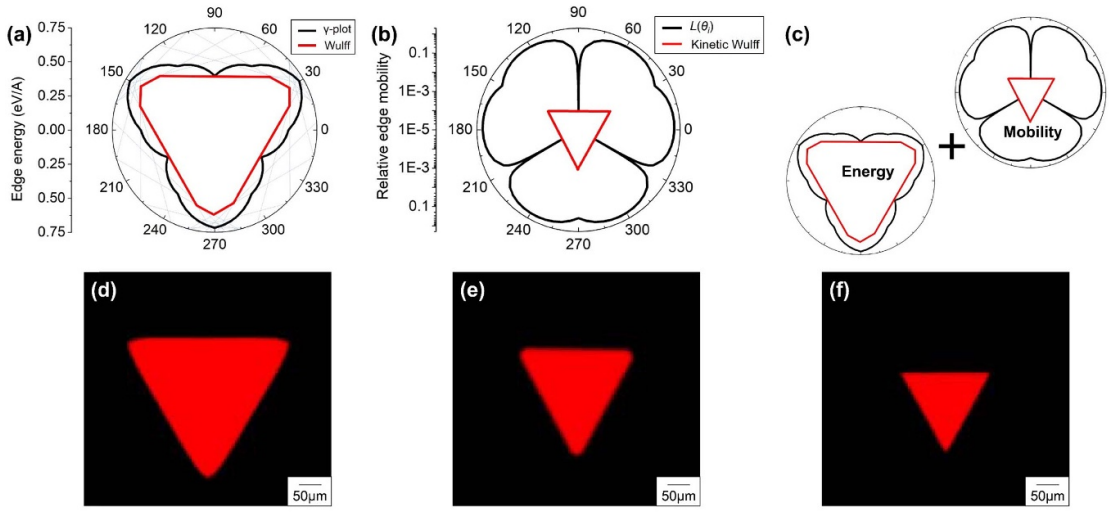

Figure 3. Theoretical predictions of h-BN island shapes on Cu (111) and corresponding phase-field simulations. (a) Orientation-dependent edge energies and Wulff constructions, the corresponding phase-field simulation result is shown in (d); (b) orientation-dependent edge mobilities and kinetic Wulff constructions, the corresponding phase-field simulation result is shown in (e); (c) both edge energy and mobility anisotropies, the corresponding phase-field simulation result is shown in (f).

anisotropy, the shape of the island is mainly triangular (figure 3(e)) since the mobility of the ZZ-N edges is significantly lower than others, which is also consistent with the kinetic Wulff construction shown in figure 3(b). With both anisotropies present, the island will grow into an equilateral triangle with sharper corners (figure 3(f)), which is consistent with experimental observations [10], confirming that the triangular h-BN islands under intermediate B:N ratio is the outcome of the interplay between edge energy and mobility anisotropies. Note that due to the symmetry of the Cu (111) surface, the diffusivities are isotropic with $D^S_{xx} = D^S_{yy}, D^S_{xy} = 0$ as shown in figures 3(c)–(f). To see the effect of anisotropic diffusivities on h-BN island morphologies, please see the virtual parametric studies included in table S1 of supplementary materials.

3.2.2. Growth on the whole substrate

Validating our model for single island growth, we further apply the phase-field model to predict the h-BN nucleation and growth on the whole substrate, assuming the substrate is a Cu single crystal with (111) surface. The whole substrate is discretized into 3600 grid points in both x- and y-directions with a grid spacing of $\Delta x = 5$ μm. The concentration distributions are taken from the large-scale model of the growth chamber. Specifically, the data for the highest diffusivity value of 10^5 cm^2 s^{-1} with different opening sizes are used (figure 2(c)). Note that since the calculated precursor concentration distributions are in 1D, they are fitted into analytical expressions as a function of position and are applied to the x-direction of the substrate in the phase-field simulation, while the distributions along the y-direction are assumed uniform. The deposition rates are assumed uniform for all simulations.

The simulated island area fraction (i.e. the coverage of the substrate) evolutions on substrates with different opening sizes are shown in figure 4(a) for growth at 1050 °C for up to 18 h, which show similar growth behaviors and can be divided into three regimes for all the cases investigated: (I) an initial incubation regime for nucleation ranging from 0.15 h for the fully open substrate to 4 h for 10 μm opening, (II) a fast nucleation-dominated regime characterized by the rapid increase in area fraction within 2 h, and finally (III) a growth and coarsening dominated regime characterized by the gradual increase of area fraction until full coverage. The overall growth kinetics are analyzed based on the Johnson–Mehl–Avrami–Kolmogorov (JMAK) equation, i.e. $f = 1-\exp(-kt^n)$; by linear fitting of ln(-ln(1 f)) vs ln t where f is the area fraction, k is a prefactor and t is time, the fitted slope is the growth index n, as shown in figure 4(b). We identified prominent differences for each growth regime, closely related to the initial precursor concentration distribution. In regime (I), the nucleation incubation time increases with the increase of the opening size; the fully open substrate requires the shortest incubation time due to the highest precursor concentration near the left boundary of the substrate (see the magenta curve in figure 2(c)). In regime (II), the slope of the area fraction curve increases with the decrease of the opening size, as quantified in figure 4(b). This phenomenon can be attributed to the fact that the precursor concentration becomes more uniform with the decrease of the opening size (see figure 2(c)), causing the precursor concentration on the whole substrate to reach the critical concentration for nucleation almost simultaneously.

On the contrary, on substrates with a large precursor concentration gradient (e.g. the fully open

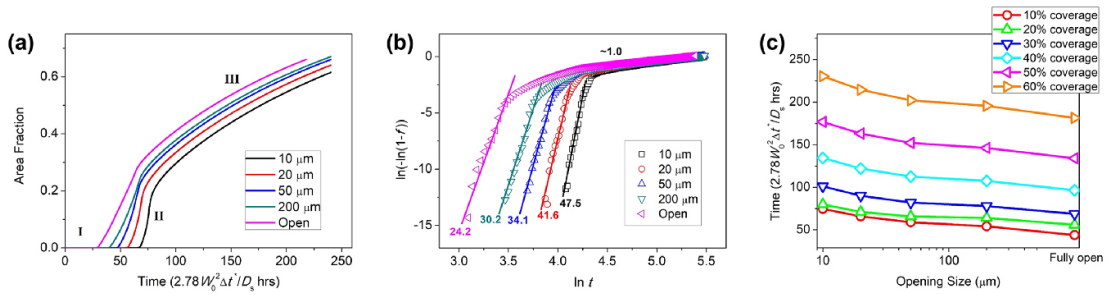

Figure 4. Substrate coverage evolution as a function time for different opening sizes. (a) Area fraction vs time showing different growth regimes. (b) JMAK analysis of the overall growth kinetics for these different opening sizes. The numbers near the fitted lines are the fitted slopes (i.e. growth indices). (c) Growth time for different island coverages as a function of opening size.

substrate), the nucleation takes place progressively from left to right following the concentration gradient, which is much slower. In regime (III), as shown in figure 4(b), the slopes of the area fraction curves are almost identical with a growth index of about 1.0, indicating a diffusion-controlled 2D growth under site-saturated conditions with island coarsening and soft-impingement. The transition from regime (II) to regime (III) is smoother for larger opening sizes due to the large precursor concentration gradient and the progressive nucleation: growth and coarsening already occur in nucleated regions before the nucleation extends throughout the substrate. Unfortunately, such detailed growth kinetics analysis has not become experimentally available to make a fair comparison with our current predictions due to the low image resolutions taken from experiments, limited image sizes compared to the size of the whole substrate, and the limited number of measurements of substrate coverage at different growth times. Nevertheless, the current study can provide semi-quantitative guidance for the experimental control of the opening size and corresponding growth time to obtain different substrate coverages, as shown in figure 4(c).

To further describe the simulated growth behaviors, we collect the growth morphologies (i.e. 2D distribution of order parameters on the substrate) during the simulation and show these morphologies at representative growth stages for the five opening sizes investigated in figure 4. Figure 5 shows the simulated h-BN morphology distribution on all the five substrates with an overall island area fraction of 10%, which corresponds to different growth times within the same growth regime (II). As shown in the morphology plots in figures 5(a)–(e) and quantified by the area fraction vs. x-coordinate plot in figure 5(f), the nucleated tiny h-BN islands distribute throughout the substrate for the opening size of 10 μm, with slightly more islands distributed on the left-hand side of the substrate due to the precursor concentration difference (see the black line in figure 2(c)); with the increase of the substrate opening size, the h-BN islands show an increasing trend to preferentially nucleate at the left-hand side of the substrates where the precursor concentration is high, due to the increase in a precursor concentration gradient. For example, for the 200 μm opening (figure 5(d)) and fully open (figure 5(e)) cases, almost no nucleation can be observed on the right half of the substrates. Meanwhile, as quantified in table 4 through statistical analysis, both the average values and standard deviations of the h-BN islands increase with the increase of the opening size of the substrate, indicating the h-BN island distribution is more uniform when the opening size is small. In addition, as shown by the inset figures in figure 5, most of the h-BN islands are triangular due to the interplay between edge energy and edge mobility anisotropies. A few trapezoids and bowtie-shaped island pairs are also observed due to competitions among adjacent islands with different orientations. These morphologies are also consistent with experimental observations [23, 52].

Similar behaviors of h-BN island distributions can be observed for the overall island area fraction of 20%, as shown in figure 6. The 20% overall area fraction is close to the transition point from growth regime (II) to (III) for substrate opening sizes of 10 μm and 20 μm, as shown in figure 4(a); the corresponding h-BN morphologies in figures 6(a) and (b) and the inserted figures show uniform distributions throughout the substrate, with almost equal area fractions in each of the 36 equal-sized sub-regions along the x-axis, as shown in figure 6(f). In comparison, for 50 μm and 200 μm openings and the fully open substrate, the nucleation-dominated growth regime (II) has not finished at 20% overall area fraction, resulting in much fewer h-BN islands near the right boundary of the substrate.

When the overall area fraction reaches 40%, all five cases have entered the growth regime (III). As shown in figure 7, triangular h-BN islands with larger sizes distribute throughout the substrates, and the island distributions are similar for all five cases. The overall average island sizes and standard deviations are also very close, as listed in table 4. However, since the initial precursor concentrations are

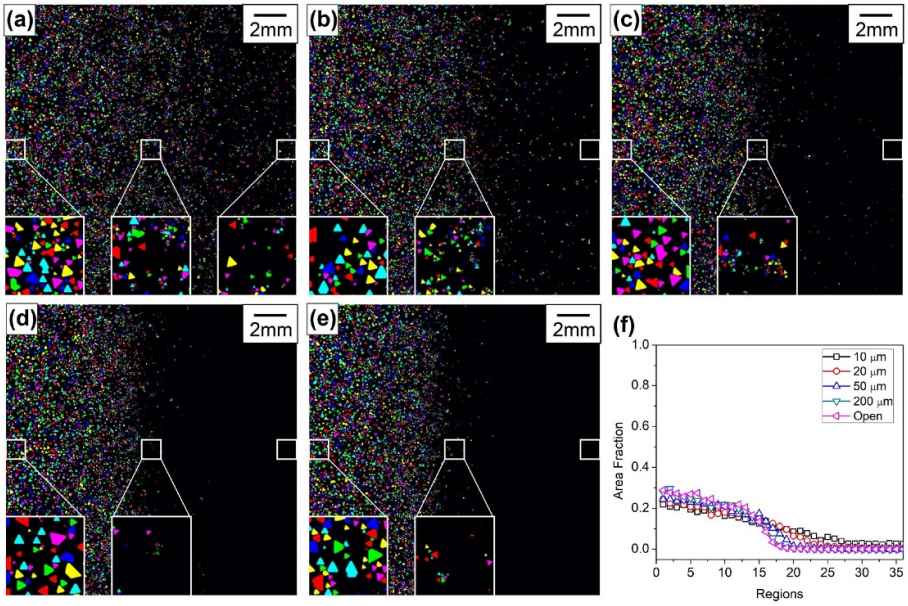

Figure 5. Simulated h-BN island morphology distribution for the overall area fraction of 10%. (a) 10 μm opening at $t = 208\,W_0^2\Delta t^*/D^s$ h; (b) 20 μm opening at $t = 184 W_0^2\Delta t^*/D^s$ h; (c) 50 μm opening at $t = 164 W_0^2\Delta t^*/D^s$ h; (d) 200 μm opening at $t = 148\,W_0^2\Delta t^*/D^s$ h; (e) fully open substrate at $t = 125\,W_0^2\Delta t^*/D^s$ h; (f) area fraction distributions along the x-axis. The substrate is divided into 36 equal-sized regions along the x-axis in this analysis. The different colors in (a)–(e) represent different island orientations. The insert figures in (a)–(e) show 5× enlarged island morphologies at three different substrate positions marked by the small square with white boundaries, respectively.

Table 4. Statistical analysis for the average values and standard deviations (in parentheses) of h-BN island sizes shown in figures 5–8.

Opening sizes	10% coverage	20% coverage	40% coverage	$t = 600\,W_0^2\Delta t^*/D^s$ hrs
10 μm	53.0 (35.1)	82.3 (39.3)	178.0 (69.5)	258.0 (107.2)
20 μm	60.5 (37.3)	77.4 (39.8)	176.1 (68.0)	267.0 (112.6)
50 μm	66.3 (40.0)	74.7 (43.9)	170.5 (69.5)	278.0 (120.4)
200 μm	71.0 (42.4)	81.4 (48.7)	169.0 (69.0)	280.9 (125.8)
Fully open	72.9 (43.6)	90.5 (51.7)	167.7 (69.7)	292.4 (132.1)

higher at the substrate's left boundary, especially for substrates with larger openings, islands first nucleated near the left boundary would have more time to undergo growth and coalescence, leading to higher volume fractions near the left boundary. This trend becomes more evident with the increase of the opening size, as shown in figure 7(f). Also, as shown by the enlarged insert figures in figures 7(a)–(e), the island sizes all become larger, and the island corners become more rounded than those in figures 5 and 6. This is due to the decrease in local supersaturation and growth driving force as the area fraction increases, leading to a decreasing trend of the role of anisotropic edge mobility in island morphology.

As the growth proceeds within a growth regime (III), the average island sizes increase, and the total number of islands decreases. This trend is manifested in figure 8 after the growth of $600 W_0^2\Delta t^*/D^s$ hrs for all five cases when the overall h-BN area fractions are higher than 70%. As quantified in figure 8(f), table 4, and figure 9(a), with the increase in opening size, the h-BN island distribution becomes less uniform, which, based on the discussions above, has been attributed to the magnitudes and distributions of precursor concentrations. As shown by the insert figures in figure 8, island sizes significantly increase while the island numbers and inter-island spacings would decrease. Adjacent islands will impinge and compete so that larger islands survive while the smaller islands will shrink and disappear; adjacent islands with the same orientation are easier to merge to form larger islands with complicated geometries since no interfacial energy exists between them. In the future, we will formulate a more accurate, misorientation-dependent expression for the parameter a using atomistic simulations, taking into account the effect of different GB types on island coalescence and coarsening.

Further growth of the islands will lead to more significant coarsening and coalescence and a further reduction in island numbers. It should be noted that when islands with different orientations impinge, another possible mechanism for coarsening is that their orientation may rotate and evolve to achieve the

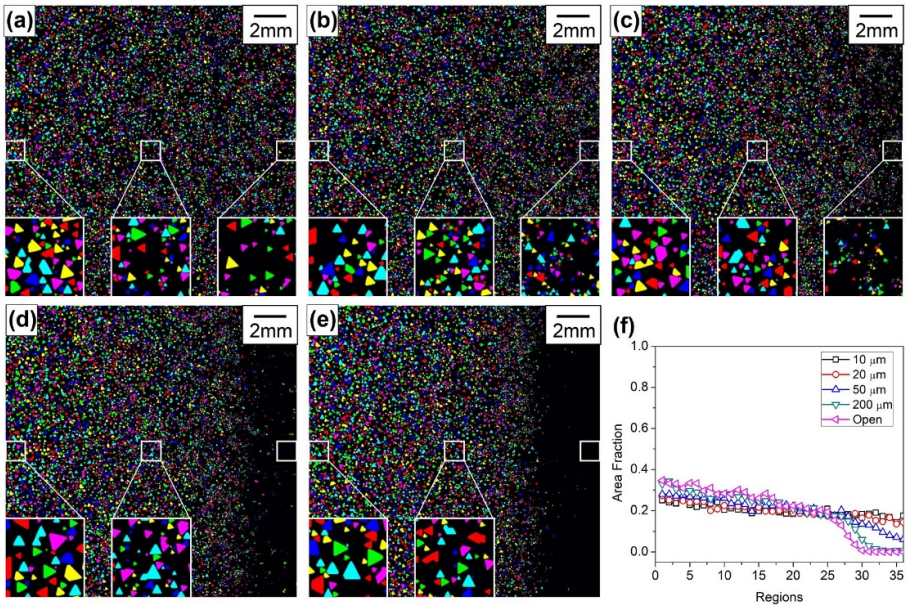

Figure 6. Simulated h-BN island morphology distribution for the overall area fraction of 20%. (a) 10 μm opening at $t = 225\,W_0^2\Delta t^*/D^s$ h; (b) 20 μm opening at $t = 196\,W_0^2\Delta t^*/D^s$ h; (c) 50 μm opening at $t = 184W_0^2\Delta t^*/D^s$ h; (d) 200 μm opening at $t = 176W_0^2\Delta t^*/D^s$ h; (e) fully open substrate at $t = 156W_0^2\Delta t^*/D^s$ h; (f) area fraction distributions along the x-axis. The substrate is divided into 36 equal-sized regions along the x-axis in this analysis. The different colors in (a)–(e) represent different island orientations. The insert figures in (a)–(e) show 5× enlarged island morphologies at three different substrate positions marked by the small square with white boundaries, respectively.

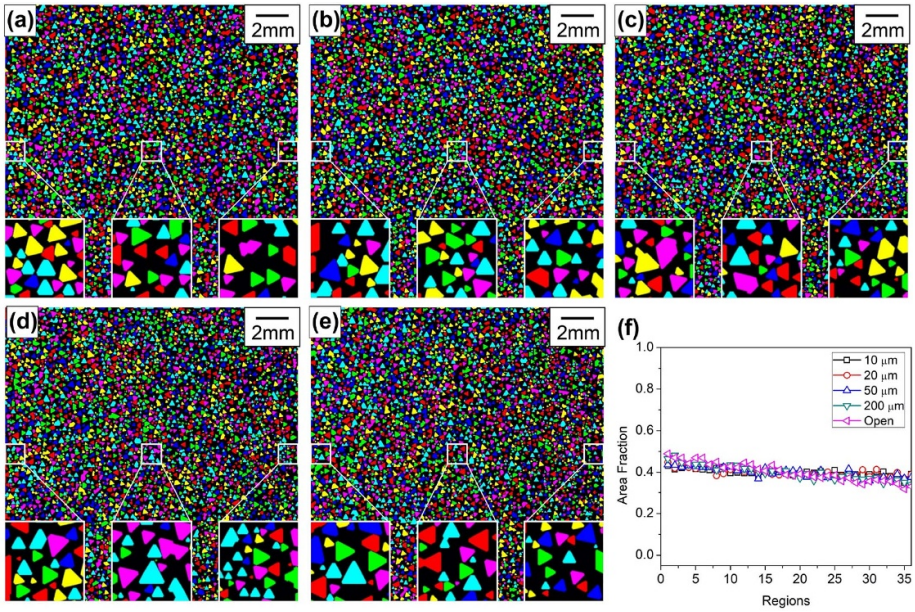

Figure 7. Simulated h-BN island morphology distribution for the overall area fraction of 40%. (a) 10 μm opening at $t = 373W_0^2\Delta t^*/D^s$ h; (b) 20 μm opening at $t = 347W_0^2\Delta t^*/D^s$ h; (c) 50 μm opening at $t = 313W_0^2\Delta t^*/D^s$ h; (d) 200 μm opening at $t = 296W_0^2\Delta t^*/D^s$ h; (e) fully open substrate at $t = 268W_0^2\Delta t^*/D^s$ h; (f) area fraction distributions along the x-axis. The substrate is divided into 36 equal-sized regions along the x-axis in this analysis. The different colors in (a)–(e) represent different island orientations. The insert figures in (a)–(e) show 5× enlarged island morphologies at three different substrate positions marked by the small square with white boundaries, respectively.

same orientations. However, we have not considered this mechanism in the current study since there is no direct experimental evidence for this mechanism during h-BN growth. Meanwhile, our current phase-field model uses different order parameters to represent different but fixed island orientations without further evolution. The Kobayashi–Warren–Carter model is suitable to deal with this problem since this model

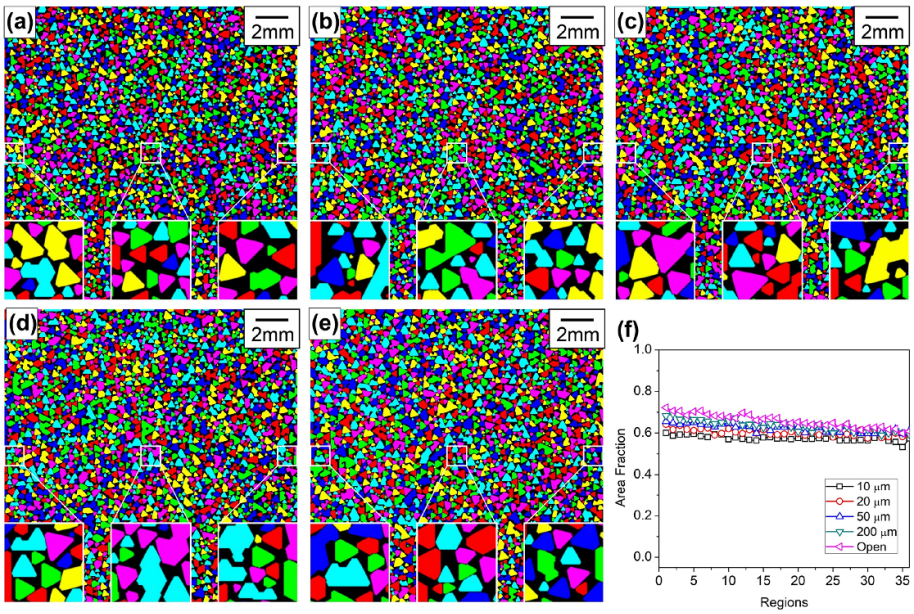

Figure 8. Simulated h-BN island morphology distribution at $t = 600W_0^2\Delta t^*/D^s$ h. (a) 10 μm opening; (b) 20 μm opening; (c) 50 μm opening; (d) 200 μm opening; (e) fully open substrate; (f) area fraction distributions along the x-axis. The substrate is divided into 36 equal-sized regions along the x-axis in this analysis. The different colors in (a)–(e) represent different island orientations. The insert figures in (a)–(e) show 5× enlarged island morphologies at three different positions of the substrate marked by the small square with white boundaries, respectively.

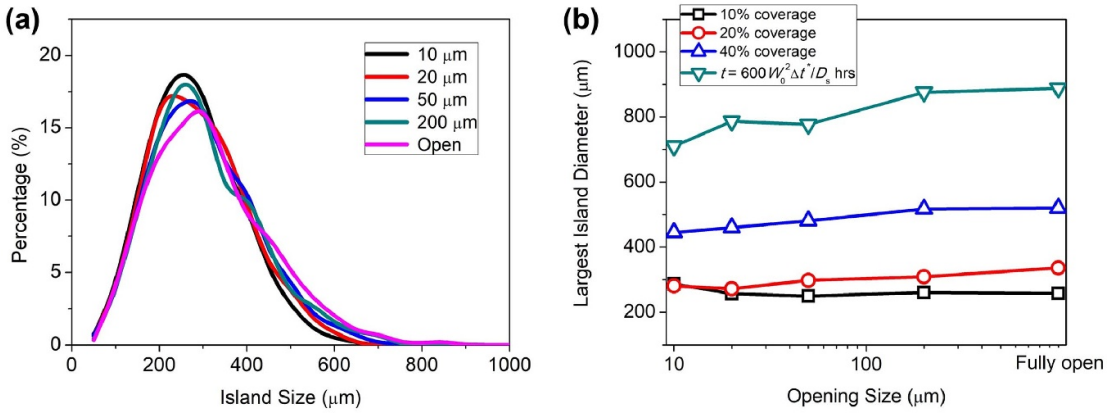

Figure 9. Simulated h-BN island size distribution for all the substrate opening sizes. (a) Island size distributions at $t = 600W_0^2\Delta t^*/D^s$h. (b) Largest island size as a function of opening size of the substrate at different substrate coverages and growth times.

introduces the grain orientation as an order parameter to evolve in different islands. We want to implement this model in the future once the rotation of impinged grains is experimentally observed and the related kinetic parameters become available.

Finally, we quantify the largest h-BN island size forms with different opening sizes for various substrate coverages and growth times, as shown in figure 9(b). The largest island size increases with the growth time (or substrate coverage) for a given substrate opening size. Under a given growth time (or substrate coverage), the largest island size increases with the increase of substrate opening size, especially when the growth time (or substrate coverage) is high. This trend is consistent with the island growth kinetics already discussed since the early growth stages (low growth time and coverage) are dominated by nucleation, while prominent growth and coarsening take place at later stages. The fully open substrate typically has the largest single domain size compared to other opening sizes under the same coverage or growth time, which can be attributed to the higher precursor concentration near the substrate's left boundary and the higher precursor concentration gradient. This precursor concentration distribution would facilitate the nucleation, growth and coarsening of h-BN islands at the left boundary of the fully open substrate, leading to larger domain sizes there.

3.2.3. Discussions

The simulations on the full substrate in section 3.2.2 show the prominent effect of substrate opening sizes on the resulting h-BN island distributions. This effect is caused by the magnitudes and gradient of the initial precursor concentration, which further affects the nucleation and growth kinetics of h-BN islands. Our results indicate that a smaller opening size leads to more uniform initial precursor concentration distributions on the substrate. Subsequently, it leads to simultaneous nucleation of h-BN islands with identical critical sizes throughout the substrate. However, in the fully open substrate, the h-BN islands sequentially nucleate downstream with a relatively more extended period (see regime (II) of figure 4). Although the standard deviation of h-BN island size increases with time (see table 4) for all cases due to the coarsening and coalescence of islands, the variation of island sizes on substrates with smaller opening sizes is still as good as that on the fully open substrate. At $t = 600W_0^2\Delta t^*/D^s$ hrs with more than 70% coverage, the island size distribution shows a similar shape for all the cases, yet the distribution's width slightly decreases with the decrease of opening size (figure 9(a)). It can also be envisioned that the differences in h-BN island distributions for different substrate opening sizes can become more significant if the growth rate (edge mobility and diffusivity) is much higher. In contrast, the nucleation and deposition rates become lower. In that case, the larger h-BN island may have already grown near the left boundary of the fully open substrate before nucleation takes place near the right boundary of the substrate; in the meantime, fewer nuclei will be introduced during the CVD process to give each other sufficient space to grow larger before impingement.

Due to the lack of accurate diffusivity data, we could not make a quantitative conversion from the phase-field simulation time to real growth time. On the other hand, given the typical CVD growth time between 0.5 and 3 h and assuming ~50% coverage can be achieved within this growth time range, we can estimate the possible range of substrate diffusivity using the equation $\Delta t = W_0^2\Delta t^*/D^s$, the parameters in table 3 and the data in figure 4(a). This value range of D^s is estimated to be 5×10^{-11} m^2 s^{-1} to 3×10^{-10} m^2 s^{-1} at the growth temperature, which can be checked once the D^s value is available from either experimental measurements or theoretical calculations.

Our results capture the same trend as reported experimentally [10], although we could not quantitatively compare the island size distribution and island growth kinetics due to lack of experimental data. The discrepancy lies in the h-BN island size: the islands show larger, more uniform sizes on the substrate with closure from experimental observations [10]. We showed that the h-BN islands have a smaller size on covered substrates, which could be due to the longer nucleation incubation time. The current study does not explicitly consider the defect distributions on the substrate, which could serve as heterogeneous nucleation sites. Furthermore, a comprehensive experimental measurement of island size distributions across the substrate at different growth times is required.

The current simulations neglect the orientation preference of the h-BN nuclei, which is experimentally confirmed for h-BN growth on Cu (111) [22]. However, for h-BN growth on Cu (100) and Cu (110), orientation selection has been reported due to the different lattice arrangement and matching between h-BN and Cu substrates [36]. Moreover, the substrate used in most existing experimental studies is polycrystalline. The growth morphology of h-BN on other lattice planes of Cu and Cu polycrystals can be predicted using the same model framework but will be left for our future studies once the edge energies and mobilities of h-BN on other crystal planes of Cu become available.

4. Conclusions

We developed a multiscale framework for modeling the growth of 2D materials using CVD-based techniques. We investigated the effect of encapsulation and closure size on nucleation and growth kinetics, morphology, size, and distributions of atomically thin h-BN on Cu (111) substrates during CVD. Our results revealed lower and more uniform precursor concentrations on the substrate for smaller opening sizes, which lead to more uniform h-BN islands. These predictions agree with existing experimental investigations. Moreover, the current study also provides the following detailed explanations of the growth behaviors of the h-BN islands.

(a) The overall growth kinetics on the substrate can be divided into three regimes dominated by different factors. Regime (I) is an incubation stage for smaller opening size (10 μm and 20 μm) and a nucleation-dominant stage for larger opening size (50 μm and 200 μm). Regime (II) is dominated by progressive nucleation until the nuclei distribute throughout the substrate. Regime (III) is dominated by growth and coarsening, while the nucleation is suppressed.

(b) The initial saturation level and precursor concentration gradient are the two critical factors determining the island size and morphology distributions by controlling the nucleation rate and nucleation number density and the time needed to complete the nucleation process throughout the substrate.

The current study also confirms that our developed multiscale computation approach can be a useful tool to investigate the effect of CVD parameters

on the growth morphology of 2D materials in general, which could be used to guide the experimental synthesis of 2D materials with desired size, shape and quality by optimizing the CVD parameters and designing CVD chambers. For example, energetic and kinetic parameters for phase-field simulations are available, the developed multiscale approach cannot only be applied to investigate and elucidate the growth morphologies and island orientation selection behaviors of 2D h-BN and TMDs (e.g. MoS_2 [53], WSe_2 [54, 55], $PdSe_2$ [56]) on various single-crystal/polycrystalline substrates, but also be applied to assist the design of more complicated growth chambers during metal-organic CVD of TMDs [57], e.g. introducing rotating substrates to obtain more uniform island growth.

Data availability statement

All data that support the findings of this study are included within the article (and any supplementary files).

Acknowledgments

Y Ji, K Momeni and L-Q Chen acknowledges the financial support from the 2D Crystal Consortium—Material Innovation Platform (2DCC-MIP) under NSF cooperative agreement DMR-1539916 and the I/UCRC Center for Atomically Thin Multifunctional Coatings (ATOMIC) seed project SP001-17. Calculations are performed using Louisiana Optical Network Initiative (LONI), the Institute for Computational and Data Sciences Advanced CyberInfrastructure (ICDS-ACI) at Penn State, and the Extreme Science and Engineering Discovery Environment (XSEDE), which National Science Foundation supports with Grant Number ACI-1548562. K Momeni also acknowledges the support from DoE-ARPA-E OPEN (DE-AR0001066), NASA-EPSCoR, the University of Alabama, and the NSF-CAREER under the NSF cooperative agreement CBET-2042683.

ORCID iD

Kasra Momeni https://orcid.org/0000-0002-4209-1129

References

[1] Cassabois G, Valvin P and Gil B 2016 Hexagonal boron nitride is an indirect bandgap semiconductor *Nat. Photon.* **10** 262–6
[2] Jo I, Pettes M T, Kim J, Watanabe K, Taniguchi T, Yao Z and Shi L 2013 Thermal conductivity and phonon transport in suspended few-layer hexagonal boron nitride *Nano Lett.* **13** 550–4
[3] Song L *et al* 2010 Large scale growth and characterization of atomic hexagonal boron nitride layers *Nano Lett.* **10** 3209–15
[4] Liu Z *et al* 2013 Ultrathin higherature oxidation-resistant coatings of hexagonal boron nitride *Nat. Commun.* **4** 1–8
[5] Bhimanapati G R *et al* 2015 Recent advances in two-dimensional materials beyond graphene *ACS Nano* **9** 11509–39
[6] Butler S Z *et al* 2013 Progress, challenges, and opportunities in two-dimensional materials beyond graphene *ACS Nano* **7** 2898–926
[7] Novoselov K S, Mishchenko A, Carvalho A and Castro Neto A H 2016 2D materials and van der Waals heterostructures *Science* **353** 6298
[8] Lee G H *et al* 2013 Flexible and transparent MoS_2 field-effect transistors on hexagonal boron nitride-graphene heterostructures *ACS Nano* **7** 7931–6
[9] Azizi A *et al* 2017 High-performance polymers sandwiched with chemical vapor deposited hexagonal boron nitrides as scalable high-temperature dielectric materials *Adv. Mater.* **29** 1–7
[10] Azizi A, AlSaud M A and Alem N 2018 Controlled growth and atomic-scale characterization of two-dimensional hexagonal boron nitride crystals *J. Cryst. Growth* **496–497** 51–6
[11] Ismach A *et al* 2012 Toward the controlled synthesis of hexagonal boron nitride films *ACS Nano* **6** 6378–85
[12] Tay R Y, Li H, Tsang S H, Zhu M, Loeblein M, Jing L, Leong F N and Teo E H T 2016 Trimethylamine borane: a new single-source precursor for monolayer h-BN single crystals and h-BCN thin films *Chem. Mater.* **28** 2180–90
[13] Babenko V, Lane G, Koos A A, Murdock A T, So K, Britton J, Meysami S S, Moffat J and Grobert N 2017 Time dependent decomposition of ammonia borane for the controlled production of 2D hexagonal boron nitride *Sci. Rep.* **7** 1–12
[14] Caneva S, Weatherup R S, Bayer B C, Brennan B, Spencer S J, Mingard K, Cabrero-Vilatela A, Baehtz C, Pollard A J and Hofmann S 2015 Nucleation control for large, single crystalline domains of monolayer hexagonal boron nitride via Si-doped Fe catalysts *Nano Lett.* **15** 1867–75
[15] Hite J K, Robinson Z R, Eddy C R and Feigelson B N 2015 Electron backscatter diffraction study of hexagonal boron nitride growth on cu single-crystal substrates *ACS Appl. Mater. Interfaces* **7** 15200–5
[16] Li J, Hu Z, Yi Y, Yu M, Li X, Zhou J, Yin J, Wu S and Guo W 2019 Hexagonal boron nitride growth on Cu-Si alloy: morphologies and large domains *Small* **15** 1–6
[17] Yang H *et al* 2019 Shape evolution of two dimensional hexagonal boron nitride single domains on Cu/Ni alloy and its applications in ultraviolet detection *Nanotechnology* **30** 245706
[18] Song X, Li Q, Ji J, Yan Z, Gu Y, Huo C, Zou Y, Zhi C and Zeng H 2016 A comprehensive investigation on CVD growth thermokinetics of h-BN white graphene *2D Mater.* **3** 035007
[19] Petrović M, Hagemann U, Horn-von Hoegen M and Meyer Zu Heringdorf F J 2017 Microanalysis of single-layer hexagonal boron nitride islands on Ir(111) *Appl. Surf. Sci.* **420** 504–10
[20] Sharma K P, Sharma S, Khaniya Sharma A, Paudel Jaisi B, Kalita G and Tanemura M 2018 Edge controlled growth of hexagonal boron nitride crystals on copper foil by atmospheric pressure chemical vapor deposition *CrystEngComm* **20** 550–5
[21] Wood G E, Laker Z P L, Marsden A J, Bell G R and Wilson N R 2017 *In situ* gas analysis during the growth of hexagonal boron nitride from ammonia borane *Mater. Res. Express* **4** aa9a7f
[22] Kim K K *et al* 2012 Synthesis of monolayer hexagonal boron nitride on Cu foil using chemical vapor deposition *Nano Lett.* **12** 161–6
[23] Stehle Y, Meyer H M, Unocic R R, Kidder M, Polizos G, Datskos P G, Jackson R, Smirnov S N and Vlassiouk I V 2015 Synthesis of hexagonal boron nitride monolayer: control of nucleation and crystal morphology *Chem. Mater.* **27** 8041–7
[24] Koepke J C *et al* 2016 Role of pressure in the growth of hexagonal boron nitride thin films from ammonia-borane *Chem. Mater.* **28** 4169–79

[25] Lee K H, Shin H J, Lee J, Lee I Y, Kim G H, Choi J Y and Kim S W 2012 Large-scale synthesis of high-quality hexagonal boron nitride nanosheets for large-area graphene electronics *Nano Lett.* **12** 714–8
[26] Ji Y, Calderon B, Han Y, Cueva P, Jungwirth N R, Alsalman H A, Hwang J, Fuchs G D, Muller D A and Spencer M G 2017 Chemical vapor deposition growth of large single-crystal mono-, bi-, tri-layer hexagonal boron nitride and their interlayer stacking *ACS Nano* **11** 12057–66
[27] Briggs N *et al* 2019 A roadmap for electronic grade 2D materials *2D Mater.* **6** 22001
[28] Zhang F, Momeni K, AlSaud M A, Azizi A, Hainey M F, Redwing J M, Chen L-Q and Alem N 2017 Controlled synthesis of 2D transition metal dichalcogenides: from vertical to planar MoS_2 *2D Mater.* **4** 025029
[29] Vilá R A, Momeni K, Wang Q, Bersch B M, Lu N, Kim M J, Chen L Q and Robinson J A 2016 Bottom-up synthesis of vertically oriented two-dimensional materials *2D Mater.* **3** 041003
[30] Momeni K *et al* 2020 Multiscale computational understanding and growth of 2D materials: a review *npj Comput. Mater.* **6** 22
[31] Zhao R, Zhao X, Liu Z, Ding F and Liu Z 2017 Controlling the orientations of h-BN during growth on transition metals by chemical vapor deposition *Nanoscale* **9** 3561–7
[32] Zhao R, Gao J, Liu Z and Ding F 2015 The reconstructed edges of the hexagonal BN *Nanoscale* **7** 9723–30
[33] Zhao R, Li F, Liu Z, Liu Z and Ding F 2015 The transition metal surface passivated edges of hexagonal boron nitride (h-BN) and the mechanism of h-BN's chemical vapor deposition (CVD) growth *Phys. Chem. Chem. Phys.* **17** 29327–34
[34] Zhang Z, Liu Y, Yang Y and Yakobson B I 2016 Growth mechanism and morphology of hexagonal boron nitride *Nano Lett.* **16** 1398–403
[35] Liu Y, Bhowmick S and Yakobson B I 2011 BN white graphene with 'colorful' edges: the energies and morphology *Nano Lett.* **11** 3113–6
[36] Liu L *et al* 2014 Unusual role of epilayer-substrate interactions in determining orientational relations in van der Waals epitaxy *Proc. Natl Acad. Sci. USA* **111** 16670–5
[37] Liu Z Q, Dong J and Ding F 2019 The geometry of hexagonal boron nitride clusters in the initial stages of chemical vapor deposition growth on a Cu(111) surface *Nanoscale* **11** 13366–76
[38] Sangiovanni D G, Gueorguiev G K and Kakanakova-Georgieva A 2018 *Ab initio* molecular dynamics of atomic-scale surface reactions: insights into metal organic chemical vapor deposition of AlN on graphene *Phys. Chem. Chem. Phys.* **20** 17751–61
[39] Liu S, van Duin A C T, van Duin D M, Liu B and Edgar J H 2017 Atomistic insights into nucleation and formation of hexagonal boron nitride on nickel from first-principles-based reactive molecular dynamics simulations *ACS Nano* **11** 3585–96
[40] Liu S, Comer J, van Duin A C T, van Duin D M, Liu B and Edgar J H 2019 Predicting the preferred morphology of hexagonal boron nitride domain structure on nickel from ReaxFF-based molecular dynamics simulations *Nanoscale* **11** 5607–16
[41] McLean B, Webber G B and Page A J 2018 Boron nitride nucleation mechanism during chemical vapor deposition *J. Phys. Chem.* C **122** 24341–9
[42] Meca E, Lowengrub J, Kim H, Mattevi C and Shenoy V B 2013 Epitaxial graphene growth and shape dynamics on copper: phase-field modeling and experiments *Nano Lett.* **13** 5692–7
[43] Momeni K, Ji Y, Zhang K, Robinson J A and Chen L Q 2018 Multiscale framework for simulation-guided growth of 2D materials *npj 2D Mater. Appl.* **2** 27
[44] Zhang K *et al* 2015 Manganese doping of monolayer MoS_2: the substrate is critical *Nano Lett.* **15** 6586–91
[45] Artyukhov V I, Liu Y and Yakobson B I 2012 Equilibrium at the edge and atomistic mechanisms of graphene growth *Proc. Natl Acad. Sci.* **109** 15136–40
[46] Geng D, Dong J, Kee A L, Ding F and Yang H Y 2019 *In situ* epitaxial engineering of graphene and h-BN lateral heterostructure with a tunable morphology comprising h-BN domains *NPG Asia Mater.* **11** 11
[47] Rajan A G, Warner J H, Blankschtein D and Strano M S 2016 Generalized mechanistic model for the chemical vapor deposition of 2D transition metal dichalcogenide monolayers *ACS Nano* **10** 4330–44
[48] Burton W K, Cabrera N, Frank F C and Francis M N 1951 The growth of crystals and the equilibrium structure of their surfaces *Phil. Trans. R. Soc.* A **243** 299–358
[49] Simmons J P, Shen C and Wang Y 2000 Phase field modeling of simultaneous nucleation and growth by explicitly incorporating nucleation events *Scr. Mater.* **43** 935–42
[50] Li X, Magnuson C W, Venugopal A, Tromp R M, Hannon J B, Vogel E M, Colombo L and Ruoff R S 2011 Large-area graphene single crystals grown by low-pressure chemical vapor deposition of methane on copper *J. Am. Chem. Soc.* **133** 2816–9
[51] Bresnehan M S, Bhimanapati G R, Wang K, Snyder D W and Robinson J A 2014 Impact of copper overpressure on the synthesis of hexagonal boron nitride atomic layers *ACS Appl. Mater. Interfaces* **6** 16755–62
[52] Wu Q, Park J H, Park S, Jung S J, Suh H, Park N, Wongwiriyapan W, Lee S, Lee Y H and Song Y J 2015 Single crystalline film of hexagonal boron nitride atomic monolayer by controlling nucleation seeds and domains *Sci. Rep.* **5** 1–8
[53] Zhang F, Wang Y, Erb C, Wang K, Moradifar P, Crespi V H and Alem N 2019 Full orientation control of epitaxial MoS_2 on hBN assisted by substrate defects *Phys. Rev.* B **99** 155430
[54] Zhang X *et al* 2019 Defect-controlled nucleation and orientation of WSe_2 on hBN: a route to single-crystal epitaxial monolayers *ACS Nano* **13** 3341–52
[55] van Duin A C T *et al* 2020 Modeling for structural engineering and synthesis of two-dimensional WSe_2 using a newly developed Reaxff reactive force field *J. Phys. Chem.* C **124** 28285–97
[56] Gu Y *et al* 2020 Two-dimensional palladium diselenide with strong in-plane optical anisotropy and high mobility grown by chemical vapor deposition *Adv. Mater.* **32** 1–10
[57] Choudhury T H, Zhang X, Al Balushi Z Y, Chubarov M and Redwing J M 2020 Epitaxial growth of two-dimensional layered transition metal dichalcogenides *Annu. Rev. Mater. Res.* **50** 155–77